

Three-Dimensional Imaging of Non-metallic Inclusions in Steel Using Ionoluminescence



SUSUMU IMASHUKU

Obtaining information on the morphology, size, distribution, and chemical composition of non-metallic inclusions in steel helps control the steel production process and the quality of the steel products. Two-dimensional analysis is commonly used to acquire this information; however, more accurate data can be obtained through three-dimensional analysis, leading to a better control of the quality of steel products and their production process. Currently, several techniques are proposed for the three-dimensional analysis of non-metallic inclusions; however, they are time consuming. Herein, the author presented a method to rapidly obtain three-dimensional images of non-metallic inclusions in steel using ionoluminescence (IL). A three-dimensional image of $\text{MgO}\cdot\text{Al}_2\text{O}_3$ spinel inclusions was constructed based on two-dimensional IL images obtained every 10 min during argon-ion bombardment. The proposed IL imaging can cover an oval-shaped area of $1.17\text{ mm} \times 0.26\text{ mm}$ on the semi-major and in the semi-minor axes, respectively, at a single measurement. Three-dimension images of $\text{MgO}\cdot\text{Al}_2\text{O}_3$ spinel inclusions with sizes more than $20\text{ }\mu\text{m}$ can be obtained within 4 hours. Therefore, the IL imaging proposed here can provide a precise and rapid account of the effects of non-metallic inclusions on steel products and the steel production process.

<https://doi.org/10.1007/s11663-024-03107-0>
© The Author(s) 2024

I. INTRODUCTION

NON-METALLIC inclusions in steel include oxides (*e.g.*, Al_2O_3 , $\text{MgO}\cdot\text{Al}_2\text{O}_3$ spinel, $\text{CaO}\cdot\text{Al}_2\text{O}_3$, and SiO_2), sulfides (*e.g.*, MnS and CaS), and nitrides (*e.g.*, AlN , BN , and TiN). These inclusions are problematic for steel products because they can induce the formation of cracks and surface defects as well as the breakage of steel wires during drawing. They can also result in hydrogen-induced cracking, fatigue failure, low ductility, and low-temperature embrittlement.^[1–3] Moreover, they can cause problems, such as nozzle clogging during continuous casting, within the steel production process.^[1–3] Thus, the analysis of non-metallic inclusions in steel is important for steel production. Because the mechanical properties of steel are largely controlled by the morphology, size, volume fraction, distribution, and chemical composition of the non-metallic inclusions, such information is investigated during the analysis of non-metallic inclusions in steel.^[4,5] The morphology, size, distribution, and chemical composition of the

non-metallic inclusions are most commonly observed in the two-dimensional cross-section of polished steel samples using optical (metallographic) microscope and a scanning electron microscope (SEM) equipped with an energy-dispersive X-ray (EDX) spectrometer.^[6,7] However, these two-dimensional analytical methods do not always reflect the actual (three-dimensional) morphology, size, and distribution of the non-metallic inclusions. For example, using two-dimensional analysis, spherical inclusions are observed as circles with diameters smaller than their actual diameters.^[8] The morphology and size of non-metallic inclusions with complicated shapes, such as oval-shaped particles and long sinuous bars, are strongly affected by the observation positions of the two-dimensional cross-section and the direction of the polish applied to the sample.^[7] Thus, three-dimensional observation of non-metallic inclusions can provide precise information on their morphology and distribution, leading to a better understanding of the effects of non-metallic inclusions on the steelmaking process and the properties of steel products.

Several analytical techniques, such as extraction method, serial sectioning, and X-ray computed tomography, are used to obtain three-dimensional morphologies and spatial distributions of the non-metallic inclusions in steels. Extraction method involves extracting non-metallic inclusions by chemically or electrolytically dissolving steels and observing the inclusions, which are collected through filtration, using optical

SUSUMU IMASHUKU is with the Institute for Materials Research, Tohoku University, 2-1-1 Katahira, Aoba-ku, Sendai, 980-8577, Japan. Contact e-mail: susumu.imashuku@imr.tohoku.ac.jp

Manuscript submitted August 28, 2023; accepted April 9, 2024.

Article published online May 7, 2024.

microscope or SEM–EDX.^[2,9] This method can provide information on the three-dimensional morphology of the non-metallic inclusions. However, the inclusions are easily destroyed before the observation, which might hinder the understanding of their actual morphology. Moreover, the spatial distribution of the non-metallic inclusions in steels cannot be obtained by extraction method. Serial sectioning is a method to construct three-dimensional images based on individual two-dimensional images obtained by continuous sectioning via mechanical polishing followed by the observation using optical microscope or SEM–EDX.^[10] Mirror polished surfaces are required to obtain each two-dimensional image, and thus, serial sectioning is time consuming. Some cutting methods are presented for serial sectioning to produce mirrored surfaces without mechanical polishing;^[11] however, obtaining three-dimensional images based on these images is still time consuming.^[10] Focused ion beam (FIB) is also used to rapidly obtain a mirrored surface of steels for serial sectioning.^[12–14] However, it can only polish areas of tens of micrometers (less than $30 \times 30 \mu\text{m}$)^[15,16] at a time, indicating that observing areas at the millimeter scale would take longer time. X-ray computed tomography can obtain three-dimensional images of non-metallic inclusions in aluminum^[17] and steel.^[18] However, this method is also time consuming^[18] and requires a synchrotron facility to use high energy X-rays that can penetrate the iron matrix, indicating that it is not an accessible method. Therefore, an analytical technique that can rapidly obtain three-dimensional images of non-metallic inclusions in steels at the laboratory scale is still required.

Ionoluminescence (IL) or ion-beam-induced luminescence imaging is used in image projection based on the phenomenon of light emission induced from materials during ion bombardment.^[19] IL is a promising method that can satisfy the abovementioned requirements for three-dimensional imaging of non-metallic inclusions in steels. Because the ion bombardment can etch materials, three-dimensional images can be constructed by intermittently capturing IL images during ion bombardment. Few studies have been reported on IL three-dimensional imaging; for example, a study was conducted for the acquisition of surface structural information of luminescent samples (*e.g.*, lapis lazuli) using IL.^[20] The author previously demonstrated that cathodoluminescence (CL) imaging, which uses the same mechanism as IL but with electron bombardment instead of ion bombardment, can provide two-dimensional images of non-metallic inclusions in steels, such as $\text{MgO}\cdot\text{Al}_2\text{O}_3$ spinel,^[21–24] Al_2O_3 ,^[21–24] calcium aluminates,^[25] rare-earth oxides (La_2O_3 , CeO_2 , and Nd_2O_3),^[26] CaS ,^[25] BN ,^[27] and AlN ^[27] inclusions. This indicates that the IL images of these non-metallic inclusions could be obtained.

The objective of this study is to present a method for rapidly obtaining three-dimensional images of non-metallic inclusions in steels using IL imaging. To establish this method, the author obtained and investigated the IL images and spectra of $\text{MgO}\cdot\text{Al}_2\text{O}_3$ spinel inclusions in Al-killed stainless-steel. $\text{MgO}\cdot\text{Al}_2\text{O}_3$ spinel inclusion is one of the most harmful inclusions for steel products and steelmaking process owing to its high

melting temperature and poor deformability.^[28–30] In particular, $\text{MgO}\cdot\text{Al}_2\text{O}_3$ spinel inclusions can cause problems during the production of stainless-steels and degrade the quality of the final products because they lead to the deterioration of the corrosion resistance of stainless-steels as well as the development of surface defects and cracks in their structures and they cause nozzle clogging during continuous casting.^[28–35] Thus, acquiring three-dimensional images of $\text{MgO}\cdot\text{Al}_2\text{O}_3$ spinel inclusions is critical for safe operation and production of stainless-steels with high cleanliness and high corrosion resistance. To the best of the author's knowledge, the proposed method is the first one to employ IL imaging for the acquisition of three-dimensional images of inclusions in steels.

II. EXPERIMENTAL

Three-dimensional IL imaging of $\text{MgO}\cdot\text{Al}_2\text{O}_3$ spinel inclusions was conducted for a model Al-killed stainless-steel sample. The model sample was prepared by melting metal powders consisting of stainless-steel (Fe, Cr, Ni, and Mn) and a metal deoxidizer (Al) under inert gas atmosphere.^[21,24,25,36] Half of a mixture of 68 mass pct electrolytic Fe powder (purity: 95 pct, Wako Pure Chemical Industries, Ltd., Osaka, Japan), 20 mass pct Cr powder (purity: 99.9 pct, Kojundo Chemical Laboratory Co., Ltd., Saitama, Japan), 10 mass pct Ni powder (purity: 99 pct, Wako Pure Chemical Industries, Ltd., Osaka, Japan), 1 mass pct Mn powder (purity: 99.9 pct, Kojundo Chemical Laboratory Co., Ltd., Saitama, Japan) were first placed in a MgO crucible, and 1 mass pct Al powder (purity: 99.9 pct, Kojundo Chemical Laboratory Co., Ltd., Saitama, Japan) was placed on the mixture. Next, the remaining half of the mixture was placed on the Al powder. The mixture for the model sample (5 g) was heated at $1560 \text{ }^\circ\text{C}$ for 30 min before being cooled to room temperature at $5 \text{ }^\circ\text{C min}^{-1}$ under Ar atmosphere at a flow rate of 200 ml min^{-1} . The surface of the model sample was polished using 600-, 1200- and 2400-grid abrasive sheets and finished using a water-free $1\text{-}\mu\text{m}$ diamond slurry.

A custom IL system was used to obtain images of the non-metallic inclusions in the model sample (Figure 1). IL images were captured using a digital mirrorless camera ($\alpha 7\text{RII}$, Sony Corp., Tokyo, Japan) equipped with a zoom lens (LZH-10A-05T, Seimitu Wave Inc., Kyoto, Japan) through a quartz viewport by bombarding the model sample with ions using an ion beam generated using an ion gun (IS 40E1, Precision and Vacuum Technology, Rogów, Poland). The detectable wavelength range of the camera was 420–680 nm. The chamber for the model samples was pumped using turbomolecular and rotary pumps to a base pressure below 2.0×10^{-5} Pa. During the ion beam bombardment, helium (purity: 99.995 pct), neon (purity: 99.999 pct), or argon (purity: 99.9999 pct) was introduced into the sample chamber, and the pressure of the chamber near the ion gun was kept at 5×10^{-4} Pa using a variable leak valve. The acceleration voltage and emission current of the ion gun were set to 5 kV and 10 mA, respectively. Luminescence spectra were also obtained

using the IL system by replacing the quartz viewport with a flange to enable the introduction of an optical fiber with a plano-convex lens at its tip. The light emitted from the model sample was collected through the optical fiber and transmitted to a spectrometer (QE65Pro, Ocean Optics Inc., Largo, Florida).

The model sample was also observed and characterized using a SEM device (TM3030 Plus, Hitachi High-Technologies Co., Tokyo, Japan) equipped with a silicon drift EDX detector (Quantax70, Bruker Corp., Billerica, Massachusetts) and an optical microscope (VHX-1000, KEYENCE Corp., Osaka, Japan).

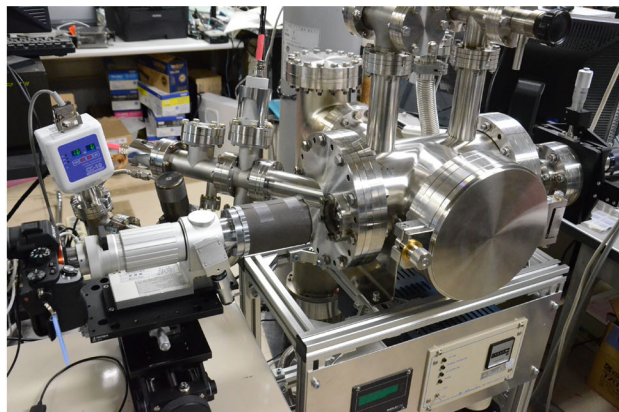
III. RESULTS AND DISCUSSION

A. Effect of Ion Species on IL Intensity

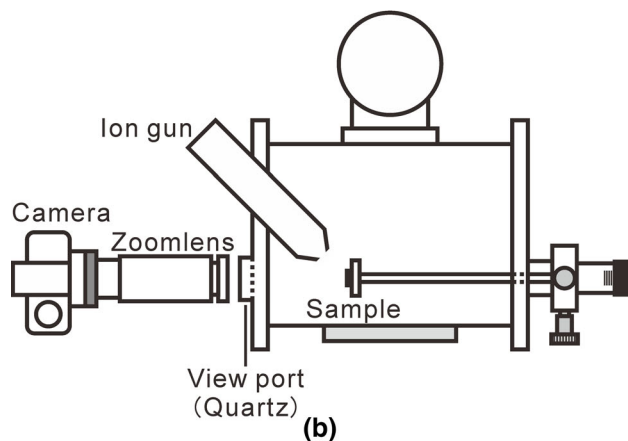
Ions of an inert gas, such as helium, neon, and argon, were used for the acquisition of IL images to prevent the reaction between the ions and the model sample. First, the luminescence spectra of $\text{MgO}\cdot\text{Al}_2\text{O}_3$ spinel were investigated to select the inert gas with the strongest luminescence intensity. The sample for used to obtain the luminescence spectra was prepared by pressing a $\text{MgO}\cdot\text{Al}_2\text{O}_3$ spinel powder (purity: 99 pct, Alfa Aesar, Ward Hill, Massachusetts) into a pellet (diameter: 30 mm

and thickness: 2 mm) at 140 MPa. The luminescence spectra that were obtained by bombarding the sample with helium, neon, and argon ions exhibited similar shapes [Figure 2(a)]. All the peaks coincided with the $\text{MgO}\cdot\text{Al}_2\text{O}_3$ spinel peaks reported in previous studies.^[23,37–39] Argon-ion bombardment provided the strongest luminescence intensities for all the detected peaks of $\text{MgO}\cdot\text{Al}_2\text{O}_3$ spinel because argon generate the highest number of ions in the chamber. Because argon has the lowest ionization energy among the ions examined in this study (*i.e.*, He: 24.59 eV, Ne: 21.56 eV, Ar: 15.76 eV), it generated the largest number of ions among them at the same accelerating voltage, emission current, and chamber pressure. Hence, argon ions were used for the acquisition of IL images in the following experiments.

During argon-ion bombardment, $\text{MgO}\cdot\text{Al}_2\text{O}_3$ spinel emitted green luminescence [Figure 2(b)], corresponding to a peak at 520 nm, which can be attributed to Mn^{2+} substituting tetrahedrally coordinated Mg^{2+} .^[37,38,40–44] The peaks observed at around 700 nm can be attributed to Cr^{3+} substituting octahedrally coordinated Al^{3+} .^[37,38,41,43] These peaks exhibited the strongest intensities among all the observed peaks; however, the luminescence corresponding to these peaks was not



(a)



(b)

Fig. 1—(a) Photograph and (b) schematic illustration of the custom IL system (Color figure online).

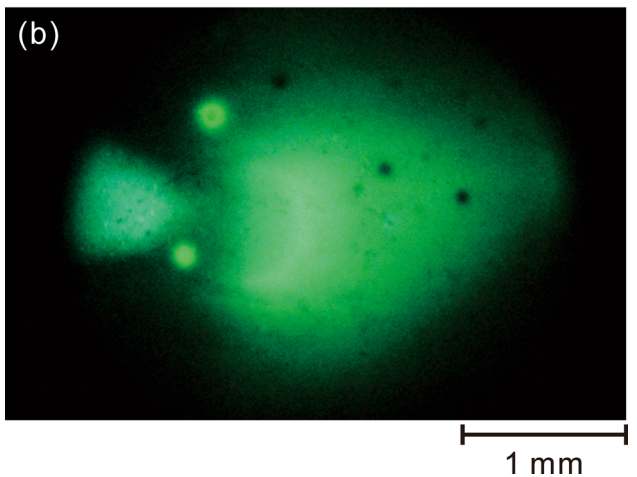
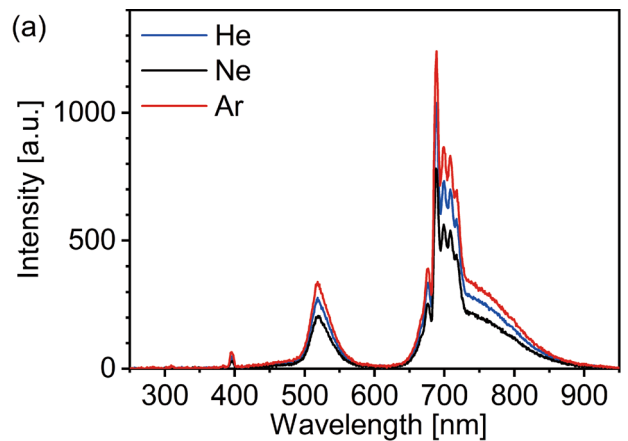


Fig. 2—(a) IL spectra obtained by bombarding the $\text{MgO}\cdot\text{Al}_2\text{O}_3$ spinel pellet with helium, neon, and argon ions (acquisition time: 1 s). (b) IL image of the $\text{MgO}\cdot\text{Al}_2\text{O}_3$ spinel pellet during argon-ion bombardment (exposure time: 1.3 s) (Color figure online).

detected because most of their wavelength regions were out of the detectable wavelength range of the camera. Thus, $\text{MgO}\cdot\text{Al}_2\text{O}_3$ spinel inclusions are expected to emit green luminescence in IL images.

Next, a dimple was formed in a specimen made of Type 304 stainless-steel, of which the composition is similar to that of the model sample, using argon-ion bombardment, and its area and depth were investigated. An oval-shaped dimple was formed after 1-hour bombardment of argon ions [Figures 3(a) and (b)]. Figures 3(c) and (d) revealed that the depth of the dimple was between 40 and 50 μm , indicating that the etching rate is approximately 0.75 $\mu\text{m min}^{-1}$ for Type 304 stainless-steel. The area of the oval-shaped dimple (depth of less than 45 μm) was stretched to 1.17 mm \times 0.26 mm on the semi-major and semi-minor axis, respectively. This area was approximately 1000 times larger than the area that can be etched by conventional FIB.

B. Three-Dimensional IL Image of $\text{MgO}\cdot\text{Al}_2\text{O}_3$ Spinel Inclusions in Model Sample

Based on the effects of the ion species on the IL intensity of $\text{MgO}\cdot\text{Al}_2\text{O}_3$ spinel, IL images of $\text{MgO}\cdot\text{Al}_2\text{O}_3$ spinel inclusions in the model Al-killed stainless-steel sample were obtained by bombarding it with argon ions.

Based on these two-dimensional IL images, a three-dimensional image of the $\text{MgO}\cdot\text{Al}_2\text{O}_3$ spinel inclusions was constructed. Figure 4 shows the region for which the IL images were obtained. The $\text{MgO}\cdot\text{Al}_2\text{O}_3$ spinel inclusions were present in areas comprising Mg and Al [Figures 4(b) and (c)], where the atomic ratios of Mg to Al were confirmed to be close to 1:2 by EDX point analysis. The presence of $\text{MgO}\cdot\text{Al}_2\text{O}_3$ spinel was also confirmed by CL analysis because the areas that emitted green luminescence and their CL spectra coincided with those illustrated in Figure 2(a), as shown in supplementary Figure S-1 (refer to Electronic Supplementary Material).

To construct a three-dimensional image of the $\text{MgO}\cdot\text{Al}_2\text{O}_3$ spinel inclusions, IL images of the model Al-killed stainless-steel sample were obtained every 10 min during argon-ion bombardment. Assuming that the model sample was etched at the same rate as Type 304 stainless-steel (0.75 $\mu\text{m min}^{-1}$), the IL images were captured at a depth interval of 7.5 μm . As shown in Figure 5, areas emitting green luminescence decreased with time, and almost all areas did not emit luminescence after bombardment for 240 min, indicating that $\text{MgO}\cdot\text{Al}_2\text{O}_3$ spinel inclusions were sputtered by the argon ions within 240 min. Based on the IL images captured every 10 min, a three-dimensional image of the

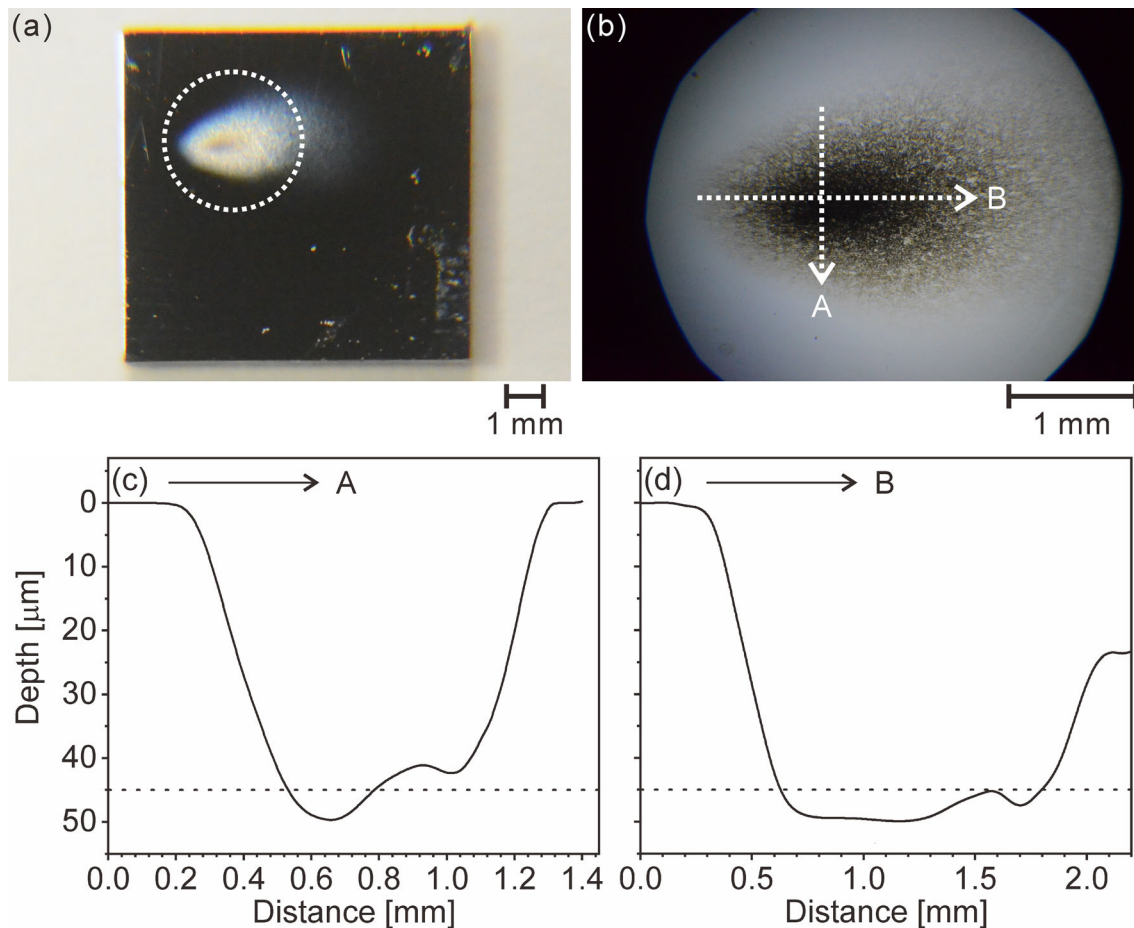


Fig. 3—(a) Photograph of Type 304 stainless-steel after 1-h bombardment of argon ions. (b) Optical microscope image of the region enclosed with the dotted line in (a). Depth profiles along the arrows (c) A and (d) in (b) (color).

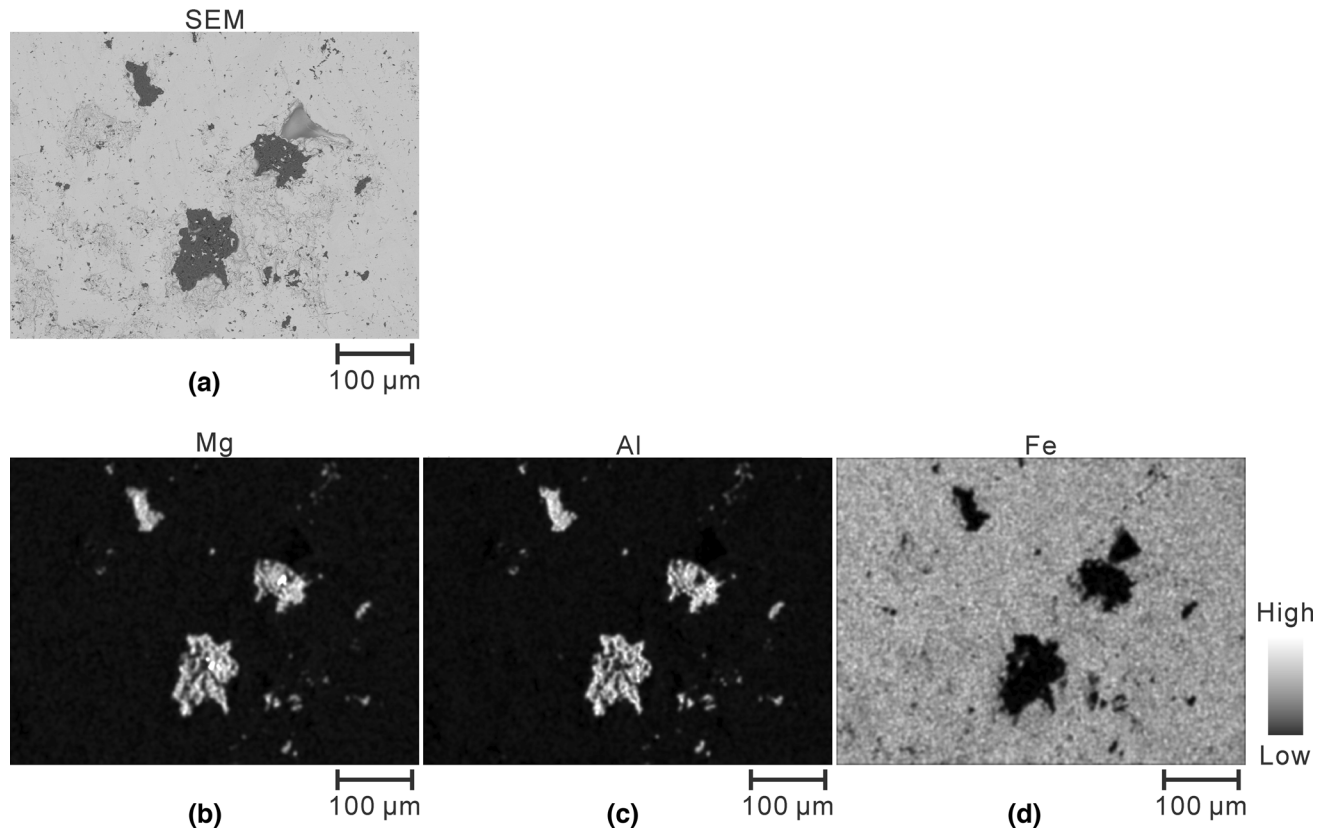


Fig. 4—(a) Backscattered electron image obtained by SEM, and EDX elemental mappings of (b) Mg, (c) Al, and (d) Fe for an area where the IL image was obtained.

MgO·Al₂O₃ spinel inclusions was constructed (Figure 6). The shape of most MgO·Al₂O₃ spinel inclusions, such as inclusions 1–4, whose sizes were more than 20 μm, (Figures 5(b) and 6) was ellipsoid, which was in good agreement with previously reported shapes of MgO·Al₂O₃ spinel inclusions in Al-killed steels.^[45–51] The morphology of the MgO·Al₂O₃ spinel inclusions changes with the progression in the steelmaking process proceeds; MgO·Al₂O₃ spinel inclusions exhibit ellipsoid or spherical shapes at the initial stage and rectangular or rhombohedron shape at the final stage.^[50] The present experimental conditions (1560 °C for 30 min) correspond to the initial stage of steelmaking. A three-dimensional image in another area of the model Al-killed stainless-steel sample also confirmed that MgO·Al₂O₃ spinel inclusions with the sizes more than 20 μm exhibited ellipsoid shapes as shown in supplementary Figure S-2 (refer to Electronic Supplementary Material). These results indicate that the present IL imaging can provide three-dimensional image of MgO·Al₂O₃ spinel inclusions with the sizes more than 20 μm. In contrast, some-size MgO·Al₂O₃ spinel inclusions, such as inclusions 5 and 6, whose sizes were approximately 10 μm, (Figures 5(b) and 6) showed a cylindrical shape, which is not a normal shape for MgO·Al₂O₃ spinel inclusions. This might be because these inclusions were not well sputtered by argon-ion bombardment. The model sample showed significant rough surface by the argon-ion bombardment for 240 min (Figure 7). Thus, these

MgO·Al₂O₃ spinel inclusions might be located in regions not reached by the argon ions, such as cleavages. Thus, to obtain precise information on the shapes of these small inclusions, the surface of the sample should be as smooth as possible during etching by conducting it at a lower beam current than the value used here. Nevertheless, the method presented here is promising for obtaining three-dimensional images of MgO·Al₂O₃ spinel inclusions in steels because appropriate information was obtained on the shapes of most MgO·Al₂O₃ spinel inclusions examined in this study. To consolidate the present IL imaging, three-dimensional images obtained using the IL imaging should be compared with those obtained using other three-dimensional imaging techniques, such as X-ray tomography, which will be future work.

The present IL imaging can obtain three-dimensional image of MgO·Al₂O₃ spinel inclusions with the sizes more than 20 μm [inclusion 1–4 in Figure 5(b)], which conventional FIB–SEM cannot analyze as the maximum area that it can measure is 30 × 30 μm. The acquisition time for the three-dimensional image of MgO·Al₂O₃ spinel inclusion was 4 hours, which is shorter than those of the extraction method, serial sectioning via mechanical polishing or cutting, and X-ray computed tomography. Although three-dimensional images of non-metallic inclusions with sizes of dozens of micrometers or less than 10 μm are critical for practical steel products, nevertheless, the present IL

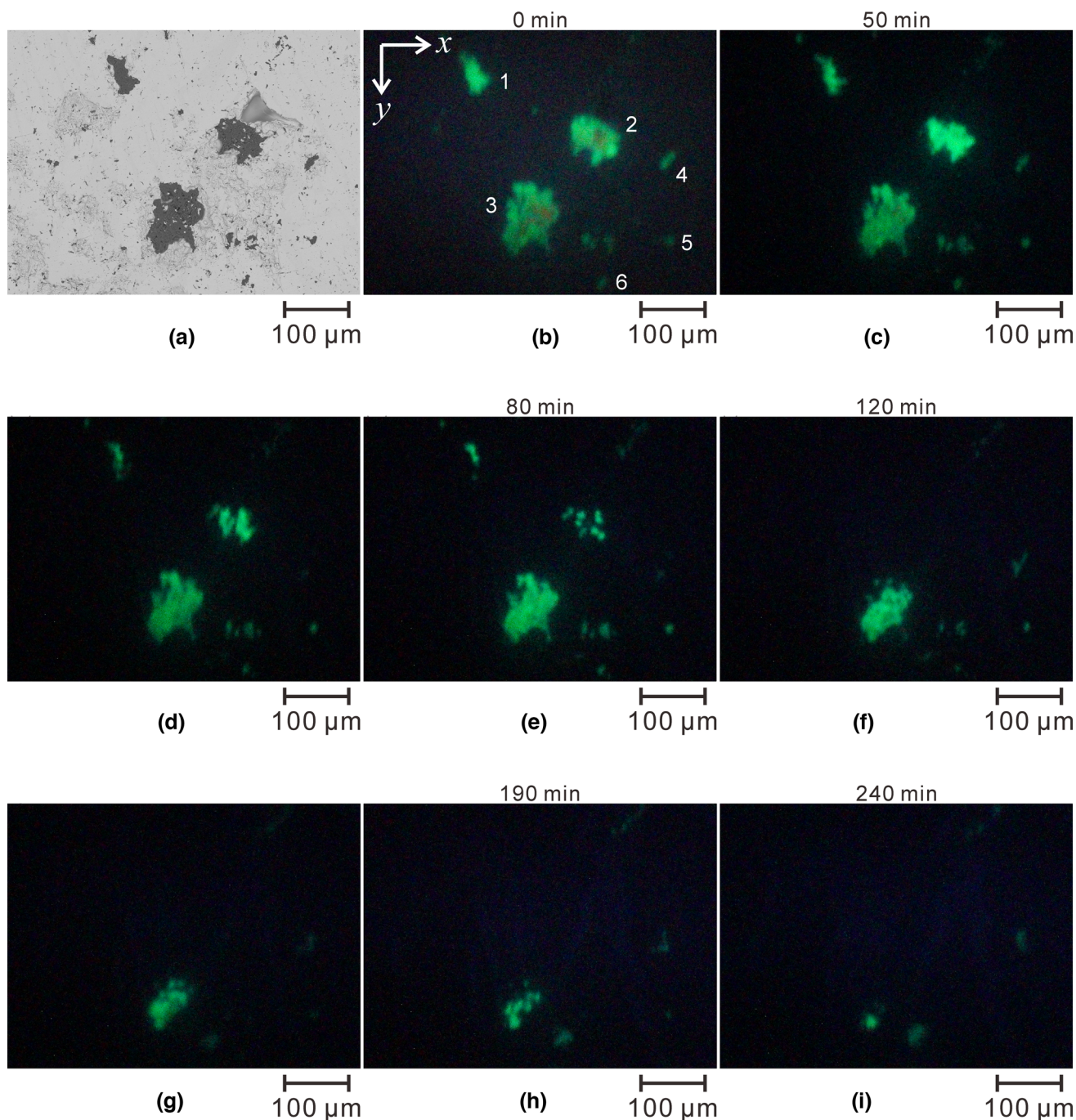


Fig. 5—(a) Backscattered electron image obtained using SEM, and the corresponding IL images obtained after argon-ion bombardment for (b) 0, (c) 50, (d) 70, (e) 80, (f) 120, (g) 160, (h) 190, and (i) 240 min (Color figure online).

imaging is the first step to realize a technique that can rapidly obtain three-dimensional images of non-metallic inclusions in steels.

IV. CONCLUSIONS

The author has proposed a method to rapidly establish three-dimensional images of $\text{MgO}\cdot\text{Al}_2\text{O}_3$ spinel inclusions in a model Al-killed stainless-steel sample based on continuous two-dimensional IL images

obtained during ion bombardment. In the IL images, the $\text{MgO}\cdot\text{Al}_2\text{O}_3$ spinel inclusions emitted green luminescence, and the argon-ion bombardment provided the highest luminescence intensity. Three-dimensional images of $\text{MgO}\cdot\text{Al}_2\text{O}_3$ spinel inclusions were obtained based on the IL images captured every 10 min while bombarding the model Al-killed stainless-steel sample with argon ions. The IL imaging presented here can cover an oval-shaped area of $1.17\text{ mm} \times 0.26\text{ mm}$ on the semi-major and semi-minor axes, respectively, at a time, and it can generate three-dimensional images of the

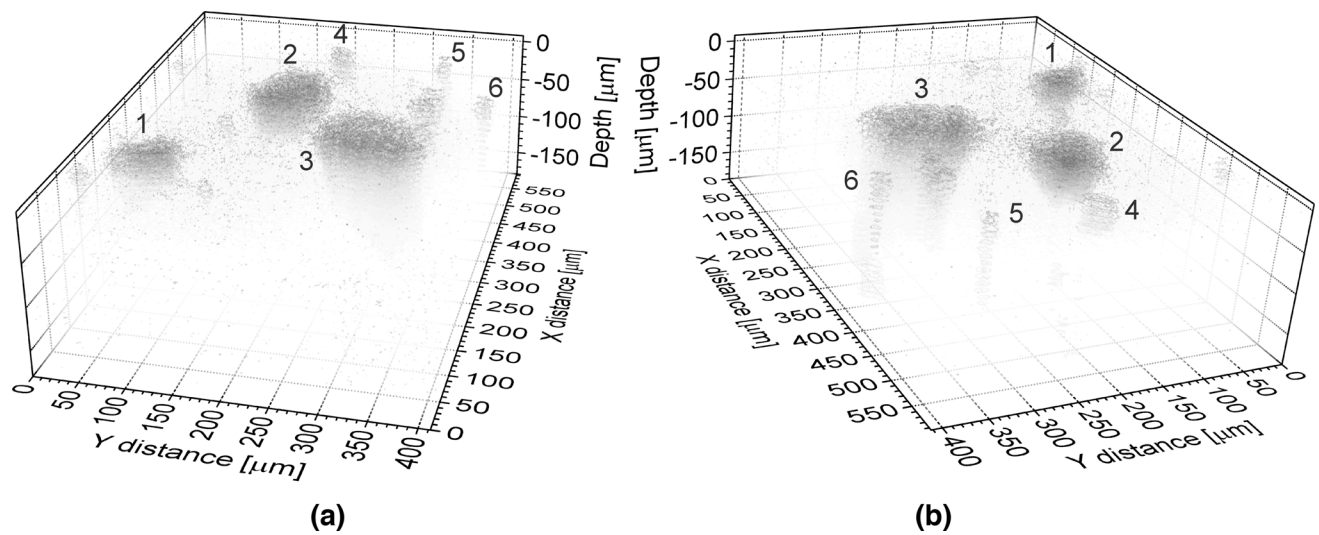


Fig. 6—Three-dimensional images of MgO-Al₂O₃ spinel inclusions in the model sample constructed based on their two-dimensional IL images from different angles. The x and y axes in the images correspond to those in Fig. 5(b).

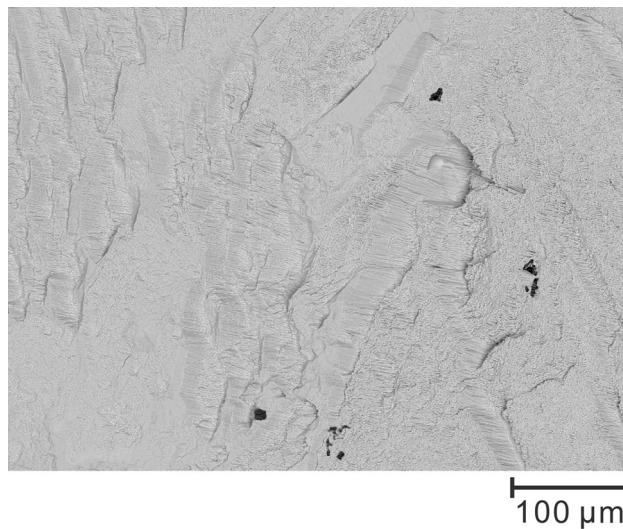


Fig. 7—SEM secondary electron image of the area where argon ions were bombarded on the model sample for 240 min.

MgO·Al₂O₃ spinel inclusions with the sizes more than 20 μm within 4 hours. Therefore, acquiring IL images is an efficient method to rapidly construct three-dimensional images of MgO·Al₂O₃ spinel inclusions in steels. In future studies, the author will investigate the applicability of the present IL imaging to other non-metallic inclusions such as Al₂O₃, CaO-Al₂O₃, BN, AlN, MnS, and CaS.

ACKNOWLEDGMENTS

Financial support for the present study was provided by JSPS KAKENHI Grant Number 22H01837. The author would like to thank to Prof. Shigeru Suzuki for lending him the optical microscope.

CONFLICT OF INTEREST

The corresponding author states that there is no conflict of interest.

OPEN ACCESS

This article is licensed under a Creative Commons Attribution 4.0 International License, which permits use, sharing, adaptation, distribution and reproduction in any medium or format, as long as you give appropriate credit to the original author(s) and the source, provide a link to the Creative Commons licence, and indicate if changes were made. The images or other third party material in this article are included in the article's Creative Commons licence, unless indicated otherwise in a credit line to the material. If material is not included in the article's Creative Commons licence and your intended use is not permitted by statutory regulation or exceeds the permitted use, you will need to obtain permission directly from the copyright holder. To view a copy of this licence, visit <http://creativecommons.org/licenses/by/4.0/>.

SUPPLEMENTARY INFORMATION

The online version contains supplementary material available at <https://doi.org/10.1007/s11663-024-03107-0>.

REFERENCES

1. H. Suito and R. Inoue: *ISIJ Int.*, 1996, vol. 36, pp. 528–36.
2. L. Zhang and B.G. Thomas: *ISIJ Int.*, 2003, vol. 43, pp. 271–91.
3. P. Kaushik, J. Lehmann, and M. Nadif: *Metall. Mater. Trans. B*, 2012, vol. 43B, pp. 710–25.

4. H.V. Atkinson and G. Shi: *Prog. Mater. Sci.*, 2003, vol. 48, pp. 457–520.
5. L.-F. Zhang: *J. Iron. Steel Res. Int.*, 2006, vol. 13, pp. 1–8.
6. M. Alba, M. Nabeel, and N. Dogan: *Steel Res. Int.*, 2019, vol. 91, p. 1900477.
7. J. Yan, T. Li, Z. Shang, and H. Guo: *Mater. Charact.*, 2019, vol. 158, pp. 3686–98.
8. T. Li, S.-I. Shimasaki, S. Taniguchi, and S. Narita: *ISIJ Int.*, 2016, vol. 56, pp. 1625–33.
9. G.R. Booker and J. Norbury: *Br. J. Appl. Phys.*, 1957, vol. 8, pp. 109–13.
10. K. Fujisaki, N. Yamashita, and H. Yokota: *Precis. Eng.*, 2012, vol. 36, pp. 315–21.
11. K. Fujisaki, H. Yokota, H. Nakatsuchi, Y. Yamagata, T. Nishikawa, T. Udagawa, and A. Makinouchi: *J. Microsc.*, 2010, vol. 237, pp. 89–95.
12. B.Y. He, O.L. Katsamenis, B.G. Mellor, and P.A.S. Reed: *Mater. Sci. Eng. A*, 2015, vol. 642, pp. 91–103.
13. D. Kumar, N.T. Nuhfer, M.E. Ferreira, and P.C. Pistorius: *Metall. Mater. Trans. B*, 2019, vol. 50B, pp. 1124–27.
14. A. Gholinia, M.E. Curd, E. Bousser, K. Taylor, T. Hosman, S. Coyle, M.H. Shearer, J. Hunt, and P.J. Withers: *Ultramicroscopy*, 2020, vol. 214, p. 112989.
15. M. Cantoni and L. Holzer: *MRS Bull.*, 2014, vol. 39, pp. 354–60.
16. T.L. Burnett, R. Kelley, B. Winiarski, L. Contreras, M. Daly, A. Gholinia, M.G. Burke, and P.J. Withers: *Ultramicroscopy*, 2016, vol. 161, pp. 119–29.
17. T. Li, S.-I. Shimasaki, S. Taniguchi, K. Uesugi, and S. Narita: *Metall. Mater. Trans. B*, 2013, vol. 44B, pp. 750–61.
18. Z. Shang, T. Li, S. Yang, J. Yan, and H. Guo: *J. Mater. Res. Technol.*, 2020, vol. 9, pp. 3686–98.
19. D. Ghose and R. Hippler, In *Luminescence of Solids*, ed. D.R. Vij (Plenum Press: New York, 1998), pp. 189–220.
20. T. Nikbakht, B. Yadollahzadeh, and M. Zahmatkesh Isfahani: *Nucl. Instrum. Methods Phys. Res. B*, 2021, vol. 489, pp. 7–10.
21. S. Imashuku, K. Ono, R. Shishido, S. Suzuki, and K. Wagatsuma: *Mater. Charact.*, 2017, vol. 131, pp. 210–16.
22. S. Imashuku, K. Ono, and K. Wagatsuma: *Microsc. Microanal.*, 2017, vol. 23, pp. 1143–49.
23. S. Imashuku and K. Wagatsuma: *X-Ray Spectrom.*, 2019, vol. 48, pp. 522–26.
24. S. Imashuku and K. Wagatsuma: *ISIJ Int.*, 2022, vol. 62, pp. 891–96.
25. S. Imashuku and K. Wagatsuma: *Metall. Mater. Trans. B*, 2018, vol. 49B, pp. 2868–74.
26. S. Imashuku and K. Wagatsuma: *Metall. Mater. Trans. B*, 2020, vol. 51B, pp. 79–84.
27. S. Imashuku and K. Wagatsuma: *Surf. Interface Anal.*, 2019, vol. 51, pp. 31–34.
28. M. Jiang, X. Wang, B. Chen, and W. Wang: *ISIJ Int.*, 2008, vol. 48, pp. 885–90.
29. J.H. Park and H. Todoroki: *ISIJ Int.*, 2010, vol. 50, pp. 1333–46.
30. S. Yang, Q. Wang, L. Zhang, J. Li, and K. Peaslee: *Metall. Mater. Trans. B*, 2012, vol. 43B, pp. 731–50.
31. K. Sakata: *ISIJ Int.*, 2006, vol. 46, pp. 1795–99.
32. J.H. Park: *Metall. Mater. Trans. B*, 2007, vol. 38, pp. 657–63.
33. Z. Deng, M. Zhu, and D. Sichen: *Metall. Mater. Trans. B*, 2016, vol. 47B, pp. 3158–67.
34. J.H. Park and Y. Kang: *Steel Res. Int.*, 2017, vol. 88, p. 1700130.
35. A. Harada, G. Miyano, N. Maruoka, H. Shibata, and S.-Y. Kitamura: *ISIJ Int.*, 2014, vol. 54, pp. 2230–38.
36. S. Imashuku: *Metall. Mater. Trans. B*, 2022, vol. 53B, pp. 190–97.
37. C.M. MacRae and N.C. Wilson: *Microsc. Microanal.*, 2008, vol. 14, pp. 184–204.
38. M. Gaft, R. Reisfeld, and G. Panczer: *Luminescence Spectroscopy of Minerals and Materials*, Springer, Berlin, 2005.
39. S. Imashuku, K. Ono, and K. Wagatsuma: *X-Ray Spectrom.*, 2017, vol. 46, pp. 131–35.
40. R. Mleak and A.H. Kitai: *J. Lumin.*, 1990, vol. 46, pp. 391–96.
41. N. Mironova, V. Skvortsova, A. Smirnovs, and L. Čugunov: *Opt. Mater.*, 1996, vol. 6, pp. 225–32.
42. R.L. Mohler and W.B. White: *Mater. Res. Bull.*, 1994, vol. 29, pp. 1109–16.
43. M. Karakus, M.D. Crites, and M.E. Schlesinger: *J. Microsc.*, 2000, vol. 200, pp. 50–58.
44. A. Tomita, T. Sato, K. Tanaka, Y. Kawabe, M. Shirai, K. Tanaka, and E. Hanamura: *J. Lumin.*, 2004, vol. 109, pp. 19–24.
45. T. Nishi and K. Shinme: *Tetsu To Hagane-J Iron Steel Inst. Jpn.*, 1998, vol. 84, pp. 97–102.
46. G. Okuyama, K. Yamaguchi, S. Takeuchi, and K.-I. Sorimachi: *ISIJ Int.*, 2000, vol. 40, pp. 121–28.
47. R. Takata, J. Yang, and M. Kuwabara: *ISIJ Int.*, 2007, vol. 47, pp. 1379–86.
48. C.-W. Seo, S.-H. Kim, S.-K. Jo, M.-O. Suk, and S.-M. Byun: *Metall. Mater. Trans. B*, 2010, vol. 41B, pp. 790–97.
49. X. Yin, Y.H. Sun, Y.D. Yang, X.F. Bai, X.X. Deng, M. Barati, and A. McLean: *Ironmak. Steelmak.*, 2016, vol. 43, pp. 533–40.
50. C. Liu, X. Gao, S.-J. Kim, S. Ueda, and S.-Y. Kitamura: *ISIJ Int.*, 2018, vol. 58, pp. 488–95.
51. D.-L. Zheng, G.-J. Ma, X. Zhang, M.-K. Liu, and Z. Li: *J. Iron. Steel Res. Int.*, 2021, vol. 28, pp. 1605–06.

Publisher's Note Springer Nature remains neutral with regard to jurisdictional claims in published maps and institutional affiliations.